ACS NANO
Cite This: ACS Nano 2019, 13, 12719−12731
www.acsnano.org

ARTICLE

Charge-Transfer-Modulated Transparent Supercapacitor Using Multidentate Molecular Linker and Conductive Transparent Nanoparticle Assembly

Jimin Choi,[†] Donghyeon Nam,[†] Dongyeeb Shin,[†] Youngkwon Song,[†] Cheong Hoon Kwon,[†] Ikjun Cho,[†] Seung Woo Lee,*[,‡] and Jinhan Cho*[,†]

[†]Department of Chemical and Biological Engineering, Korea University, 145 Anam-ro, Seongbuk-gu, Seoul 02841, Republic of Korea

[‡]School of Mechanical Engineering, Georgia Institute of Technology, Atlanta, Georgia 30332-0245, United States

Supporting Information

ABSTRACT: One of the most critical issues in preparing high-performance transparent supercapacitors (TSCs) is to overcome the trade-off between areal capacitance and optical transmittance as well as that between areal capacitance and rate capability. Herein, we introduce a TSC with high areal capacitance, fast rate capability, and good optical transparency by minimizing the charge transfer resistance between pseudocapacitive nanoparticles (NPs) using molecular linker- and conductive NP-mediated layer-by-layer (LbL) assembly. For this study, bulky ligand-stabilized manganese oxide (MnO) and indium tin oxide (ITO) NP multilayers are LbL-assembled through a ligand exchange reaction between native ligands and small multidentate linkers (tricarballylic acid). The introduced molecular linker substantially decreases the separation distance between neighboring NPs, thereby reducing the contact resistance of electrodes. Moreover, the periodic insertion of ITO NPs into the MnO NP-based electrodes can lower the charge transfer resistance without a meaningful loss of transmittance, which can significantly improve the areal capacitance. The areal capacitances of the ITO NP-free electrode and the ITO NP-incorporated electrode are 24.6 mF cm^{-2} (at 61.6% transmittance) and 40.5 mF cm^{-2} (at 60.8%), respectively, which outperforms state of the art TSCs. Furthermore, we demonstrate a flexible symmetric solid-state TSC that exhibits scalable areal capacitance and optical transmittance.

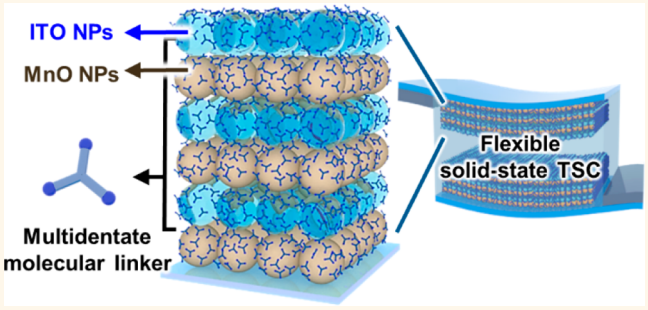

KEYWORDS: *transparent supercapacitor, indium tin oxide nanoparticles, multidentate linker, charge transfer resistance, multilayer*

Recently, considerable attention has been paid to transparent electronic devices, which can be used in many emerging applications, such as electrochromic windows, smart watches, and other next-generation electronic glassworks, leading to the strong demand for the development of various transparent component parts.[1−8] Most studies have been directed toward the fabrication of transparent displays, light-emitting diodes, and electronic circuits and consequently have produced numerous advances to date. Despite this progress, relatively little research effort has been focused on the utilization of transparent power sources that are required for the ultimate realization of self-powered, fully transparent integrated devices. In particular, transparent supercapacitors (TSCs) have been investigated as one of the promising candidates for self-powered next-generation transparent devices due to their advantages, including high power density and long cycle life. However, the low energy performance indices (particularly poor areal capacitance ∼ capacitance per unit area, F cm^{-2}) of TSCs, which result from the surface-limited charge storage mechanism and ultrathin electrode thicknesses, are critical barriers to developing practical TSCs. The most common carbon-material-based TSCs show a thickness-dependent optical transmittance of 30−85% at 550 nm, but their areal capacitances usually do not exceed 4 mF cm^{-2} due to the electric double-layer capacitance of carbon

Received: June 12, 2019
Accepted: October 18, 2019
Published: October 23, 2019

DOI: 10.1021/acsnano.9b04594
ACS Nano 2019, 13, 12719−12731

Scheme 1. Schematic illustration of the formation of a transparent supercapacitor electrode based on pseudocapacitive OA-MnO NPs and conductive/transparent OAm-ITO NPs using multidentate small-linker-mediated ligand exchange reaction.

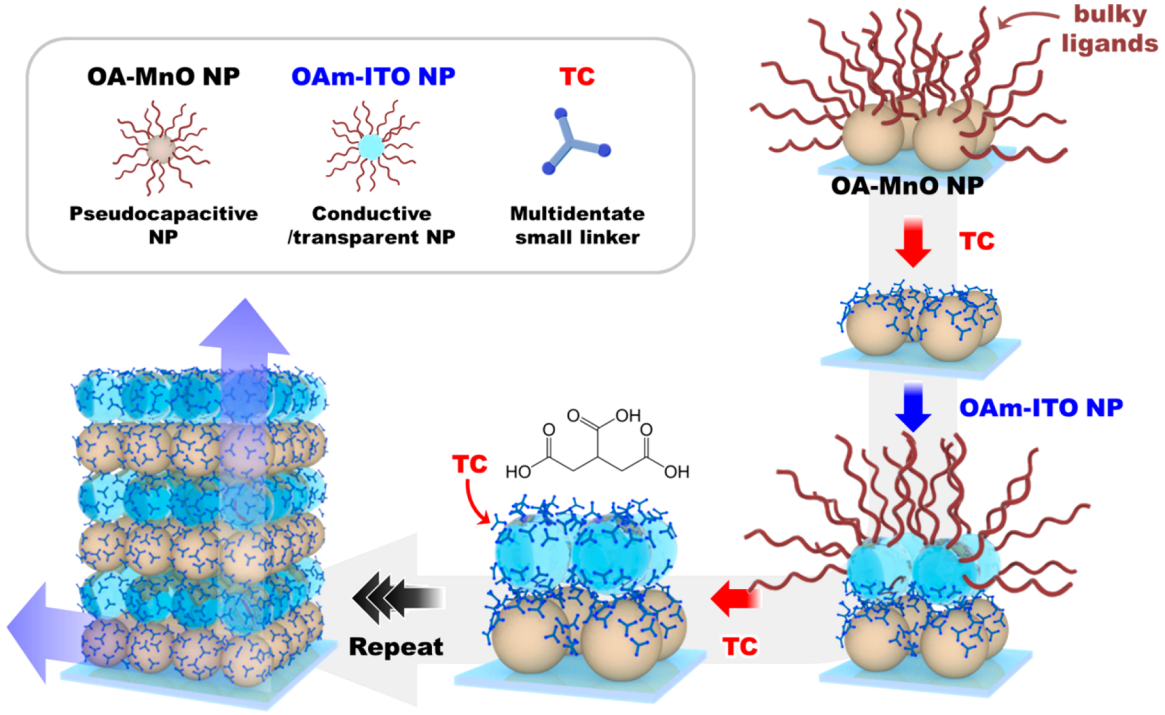

materials.[9−14] For example, Chen *et al.*[14] reported that wrinkled graphene-based TSCs exhibited an areal capacitance of approximately 6 μF cm^{-2} with an optical transmittance of 57% at 550 nm. Additionally, when the loading amount of the carbon materials is increased to improve areal capacitance, the transmittance of the electrode is significantly reduced because of the light absorption and scattering of the active components, implying a trade-off between optical transparency and areal capacitance.

As an alternative, high-energy pseudocapacitive (PC) nanoparticles (NPs) have been used for the preparation of high-performance TSCs that can provide relatively high areal capacitance with ultrathin film thickness (*i.e.*, high optical transmittance).[15−24] In particular, Liu *et al.*[16] reported that MnO_2 nanoflakes electrochemically deposited onto highly transparent Ni mesh films exhibited an outstanding areal capacitance of 80.7 mF cm^{-2} (on the basis of a half-cell electrode) and a high optical transmittance of 84%. In this case, however, the areal capacitance was calculated using only the narrow area of the patterned micrometer-scale Ni string with a large void area, which could not represent a practical capacitance value (*i.e.*, areal capacitance based on the entire device). Ma *et al.*[24] also reported that the transparent carbon-fiber-based electrode with electrodeposited MnO_2 exhibited a high areal capacitance of 8 mF cm^{-2} with a transmittance of 58% (on the basis of a full cell) and improved the areal capacitance up to 35.8 mF cm^{-2} through control of the electrodeposition time of MnO_2. More recently, Wang *et al.*[18] reported that island-like patterned MnO_2 array-based electrodes delivered a high areal capacitance of 3.5 mF cm^{-2} (on the basis of a half-cell electrode) with an optical transmittance of 69%. Despite the high-energy performance of PC materials, most PC-material-based electrodes have poor electrical conductivity; thus, the charge transfer resistance of PC-material-based electrodes increases with increasing loading amount. As a result, these phenomena significantly reduce the rate capability and optical transmittance of the electrode.[25,26]

To lower the charge transfer resistance, various conducting components, such as carbon-based materials or conducting polymers, have been incorporated into PC-material-based supercapacitor electrodes through physical adsorption processes such as simple solution casting or blending.[27−30] However, in most cases, conductive materials have strong light absorption (mainly because of carbon nanotubes (CNTs) and/or graphene), which restricts the enhancement in optical performance and energy storage of TSCs. Additionally, it should be noted that the above-mentioned physical adsorption processes provide poor control over the loading amount (or thickness) of components as well as homogeneous blending at the nanoscale, which leads to much difficulty in precisely controlling the trade-off between energy storage performance and optical transparency.

Layer-by-layer (LbL) assembly is a simple fabrication process that has been widely used for the preparation of ultrathin nanocomposite films with tailored thicknesses, compositions, and functionalities on various substrates by utilizing complementary interactions between different components.[31−42] In particular, in the case of electrostatic LbL assembly for energy storage applications, most studies have mainly focused on supercapacitor electrodes composed of charged carbon materials (*e.g.*, cationic NH_3^+-functionalized CNT or -reduced graphene oxide) and oppositely charged materials (*e.g.*, anionic COO^--functionalized carbon materials, electrochemically active polymers, PC NPs, or bulky polymer linkers) using complementary electrostatic interactions in aqueous media.[40−42] Despite the promising architectures obtainable by conventional LbL assembly, electrostatic LbL assembly of TSC electrodes possesses some critical limitations, including (1) low packing density (<30%) of PC NPs per layer due to the reciprocal electrostatic repulsion between same-

DOI: 10.1021/acsnano.9b04594
ACS Nano 2019, 13, 12719−12731

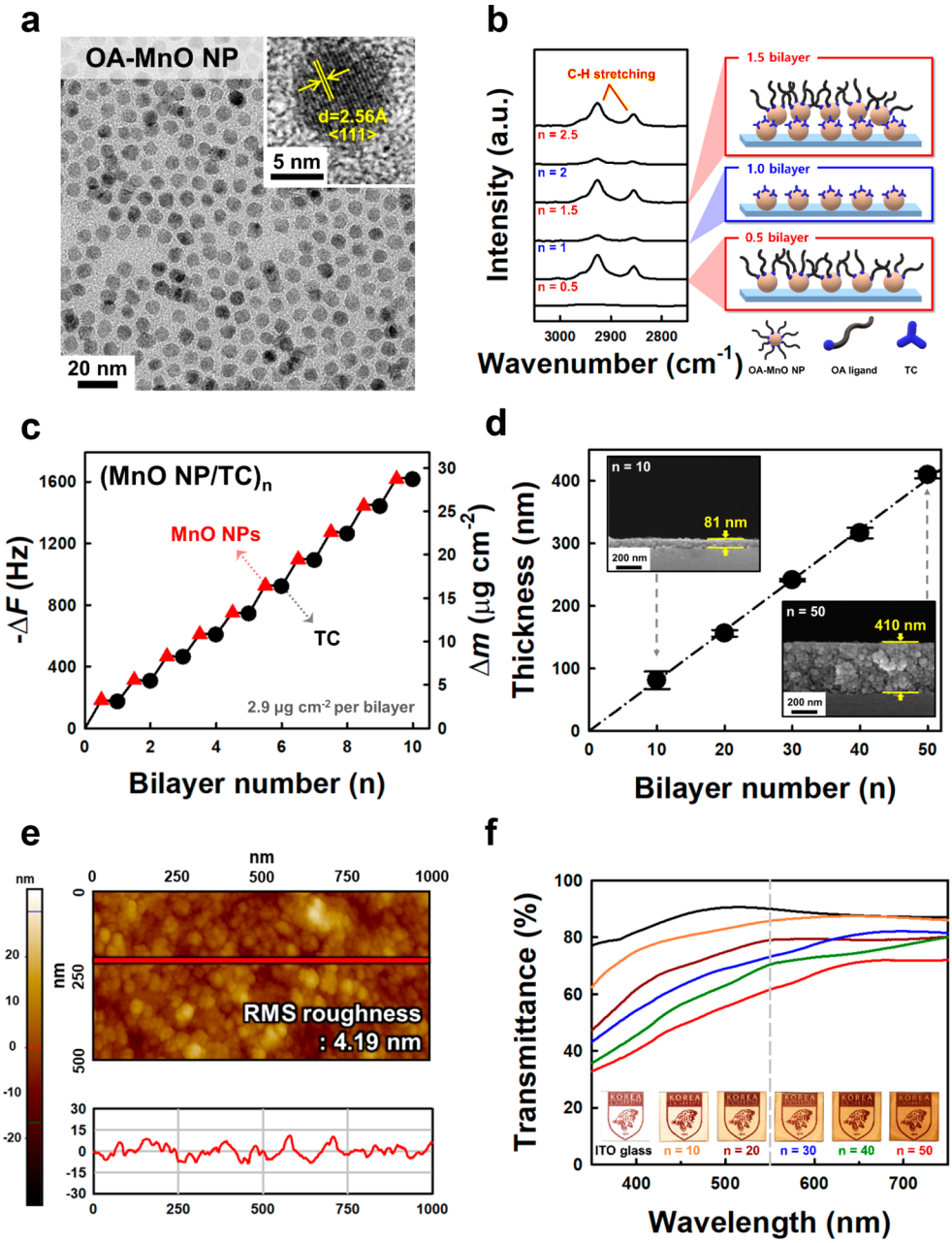

Figure 1. (a) HR-TEM images of synthesized OA-MnO NPs. (b) ATR-FTIR spectra and schematic representation of $(MnO\ NP/TC)_n$ multilayers as a function of bilayer number (n). (c) Frequency and mass change of $(MnO\ NP/TC)_n$ multilayers obtained from QCM measurements as a function of bilayer number. (d) Thickness change of $(MnO\ NP/TC)_n$ multilayers measured from the cross-sectional FE-SEM images (insets). (e) AFM image and rms surface roughness of $(MnO\ NP/TC)_{50}$ multilayer. (f) Transmittance spectra and digital images of the $(MnO\ NP/TC)_n$ multilayers on ITO glass with different bilayer number (n). The university logos were used with permission from Korea University.

charged PC NPs,[43,44] (2) strong light absorption of carbon-based materials, and/or (3) high contact resistance originating from the insulating organics (more specifically, bulky charged polymer linkers) sandwiched between electrochemically active components. As a result, these drawbacks act as a major obstacle to preparing high-performance TSCs.

Herein, we introduce a high-performance TSC with high areal capacitance, excellent rate capability, and good optical transmittance using an unconventional LbL assembly between high-energy PC NPs (*i.e.*, MnO NPs) and conductive/transparent NPs (*i.e.*, indium tin oxide (ITO) NPs) in organic media without using any carbon-based materials or conducting polymers (Scheme 1). In particular, we highlight that our approach can provide an alternative for effectively alleviating the complex and troublesome trade-off between areal capacitance and optical transmittance as well as that between areal capacitance and rate capability. For this study, oleic acid (OA)-stabilized MnO NPs (OA-MnO NPs) with a diameter of 10 ± 0.5 nm and oleylamine (OAm)/octanoic acid (OCA)-stabilized ITO NPs (OAm-ITO NPs) with a diameter of 7 ± 2 nm were prepared in toluene and then were LbL-assembled with tricarballylic acid (TC, $M_w \approx 176$) serving as a multidentate linker in ethanol. In this LbL assembly process, bulky and native ligands (*i.e.*, OA, OAm, and OCA ligands)

DOI: 10.1021/acsnano.9b04594
ACS Nano 2019, 13, 12719−12731

loosely bound to the surface of the MnO and ITO NPs are replaced by multidentate TC with three carboxylic acid (COOH) groups through a ligand exchange reaction without additional chemical or thermal treatments during LbL deposition. Based on this ligand exchange reaction, a variety of LbL-assembled $(MnO\ NP/TC)_n$, $(ITO\ NP/TC)_n$, and $(MnO\ NP/TC/ITO\ NP/TC)_m$ multilayer films were deposited onto ITO glass or flexible ITO-coated poly(ethylene terephthalate) (PET) substrates to obtain TSCs. We also demonstrate that the COOH-functionalized small molecule is capable of directly bridging all the interfaces between NPs as a multidentate organic linker, which can effectively reduce the contact resistance between neighboring NPs. Another feature is that ITO NPs themselves have electrical conductivity as well as transparency, and furthermore the alternating LbL assembly of MnO and ITO NPs significantly increases the areal capacitance and rate capability without considerably sacrificing optical transmittance.

In particular, in the case of ITO NP-incorporated MnO NP films (*i.e.*, $(MnO\ NP/TC/ITO\ NP/TC)_{50}$ multilayers), their areal capacitance can be increased up to 40.5 mF cm^{-2} at a current density of 0.1 mA cm^{-2}, which outperforms the areal capacitances of LbL-assembled electrodes without ITO NPs (24.6 mF cm^{-2} at 0.1 mA cm^{-2}) and most TSCs reported to date. On the other hand, the optical transmittance of $(MnO\ NP/TC/ITO\ NP/TC)_{50}$-coated ITO glass is approximately 60.8%, which is fairly similar to the transmittance of 61.6% measured from the $(MnO\ NP/TC)_{50}$-coated ITO glass. We also highlight that the areal capacitance and optical transparency of these LbL-assembled TSCs can be easily but exactly controlled using the layer number. Furthermore, the flexible and symmetric solid-state TSCs based on the $(MnO\ NP/TC/ITO\ NP/TC)_m$ multilayers exhibit high areal performances and good optical transparency. Given that our approach using ligand-exchange-based LbL assembly and conductive/transparent NPs can significantly improve the performance of TSCs without a notable loss of transmittance, our approach can provide an important basis for designing various electrodes for electrochemical applications, including electrochromic films requiring facile charge transfer and high optical transparency.

RESULTS AND DISCUSSION

For the preparation of TSC electrodes, we first synthesized well-defined OA-MnO NPs with a diameter of approximately 10 nm that can be well dispersed in nonpolar media such as toluene, as shown in the high-resolution transmission electron microscopy (HR-TEM) image (Figure 1a). When these OA-MnO NPs were deposited onto the outermost TC-coated substrates, OA with one carboxylate ion (COO^-) group loosely bound to the MnO NP surface was easily replaced by small multidentate TC linkers *via* a ligand exchange reaction during deposition, which was demonstrated using Fourier transform infrared (FTIR) spectroscopy (Figure 1b and Figure S1). First, the FTIR spectrum of OA-MnO NPs displayed two prominent absorption peaks (C−H stretching at 2926−2854 cm^{-1}) derived from the long alkyl chains of the bulky OA ligand, while TC had no absorption peak in the corresponding wavenumber range. Generally, when the OA ligands with the COOH group are adsorbed onto the surface of MnO NPs, the COO^- stretching peak (at 1585 and 1465 cm^{-1}) appears in place of the C═O stretching (at 1720 cm^{-1}) peak from the COOH group. These absorption peaks of the OA ligands exactly overlapped with those of the TC linkers before and after adsorption onto the surface of MnO NPs. Therefore, the ligand exchange reaction between OA and TC was determined through the trace of the absorption peak arising from the long alkyl chains of the OA ligands. More specifically, when TC was deposited onto the OA-MnO NP-coated substrate (*i.e.*, the substrate/OA-MnO NP defined as "n = 0.5" in Figure 1b) through the ligand exchange reaction, the C−H stretching peak intensity of the outermost OA ligands bound to the MnO NP surface significantly decreased (*i.e.*, the substrate/(MnO NP/TC) defined as "n = 1" in Figure 1b). As the OA-MnO NP layer was further adsorbed onto the outermost TC-coated film, the absorption peak intensity of the C−H stretching peaks increased again. That is, alternating deposition of TC and OA-MnO NPs results in inversely correlated changes in the intensities of the C−H stretching peak, indicating that the OA ligands bound to the surface of MnO NPs were exchanged with TC.

Although the carboxylate ion ($-COO^-$) group of the OA ligand acts either as a bidentate ligand that binds to Mn^{2+} *via* two O atoms or as a monodentate ligand that links to Mn^{2+} *via* only one O atom,[36,45] it is clear that the TC linker with three COOH groups can serve as a multidentate ligand. It was reported that multidentate ligands possess more stable and stronger binding affinity for the surface of NPs than conventional mono- and/or bidentate ligands.[37,46] Additionally, considering that the pK_a (pK_a = 9.1−9.5) of the COOH group of native OA ligands with long alkyl chains is higher than that (pK_a = 3.49) of the COOH groups of TC (*i.e.*, three carboxylic acid (COOH) groups per TC molecule), we cannot exclude the possibility that the ligand exchange reaction observed in our approach can slightly depend on the degree of acidity of COOH groups.[47] As a result, compared to the OA ligands with weak acidity and mono- or bidentate binding, the multidentate TC ligands with stronger acidity can provide enhanced coordination interactions with the surface of MnO NPs. These possible explanations also suggest that other bulky mono/bidentate ligands (with amine (NH_2) groups as well as COOH groups) bound to the surface of transition metal oxide NPs can also be exchanged with the multidentate TC linker during LbL deposition (a more detailed explanation will be given in a later part). Furthermore, it should be noted that this adsorption mechanism induces densely packed MnO NP arrays by reducing the interparticle distance between neighboring MnO NPs since one TC layer can directly bridge the MnO NP−MnO NP interface.

Next, we quantitatively investigated the vertical growth of $(MnO\ NP/TC)_n$ multilayers with increasing bilayer number (n). In this case, the concentrations of OA-MnO NP and TC solutions used for LbL assembly were 10 and 2 mg mL^{-1}, respectively. Figure 1c shows the frequency change ($-\Delta F$) and the mass change (Δm) in the adsorbed OA-MnO NPs and TC due to the increase in the number of bilayers. The mass change was calculated from the frequency change during the adsorption of the OA-MnO NPs and TC on quartz crystal microbalance (QCM) electrodes using the Sauerbrey equation (see the Experimental Section). The alternating deposition of OA-MnO NP and TC resulted in $-\Delta F$ values of 169 ± 18 (Δm of ~3.0 $\mu g\ cm^{-2}$) and −7.2 ± 3 Hz (Δm of ~−0.13 $\mu g\ cm^{-2}$) per layer, respectively. In this case, the decreased mass change derived from TC adsorption was mainly caused by the ligand exchange reaction between the bulky OA ligands ($M_w \approx 282$) and the small TC linkers ($M_w \approx 176$). The mass ratio of pure inorganic components (*i.e.*, MnO NPs) in the multilayer

DOI: 10.1021/acsnano.9b04594
ACS Nano 2019, 13, 12719−12731

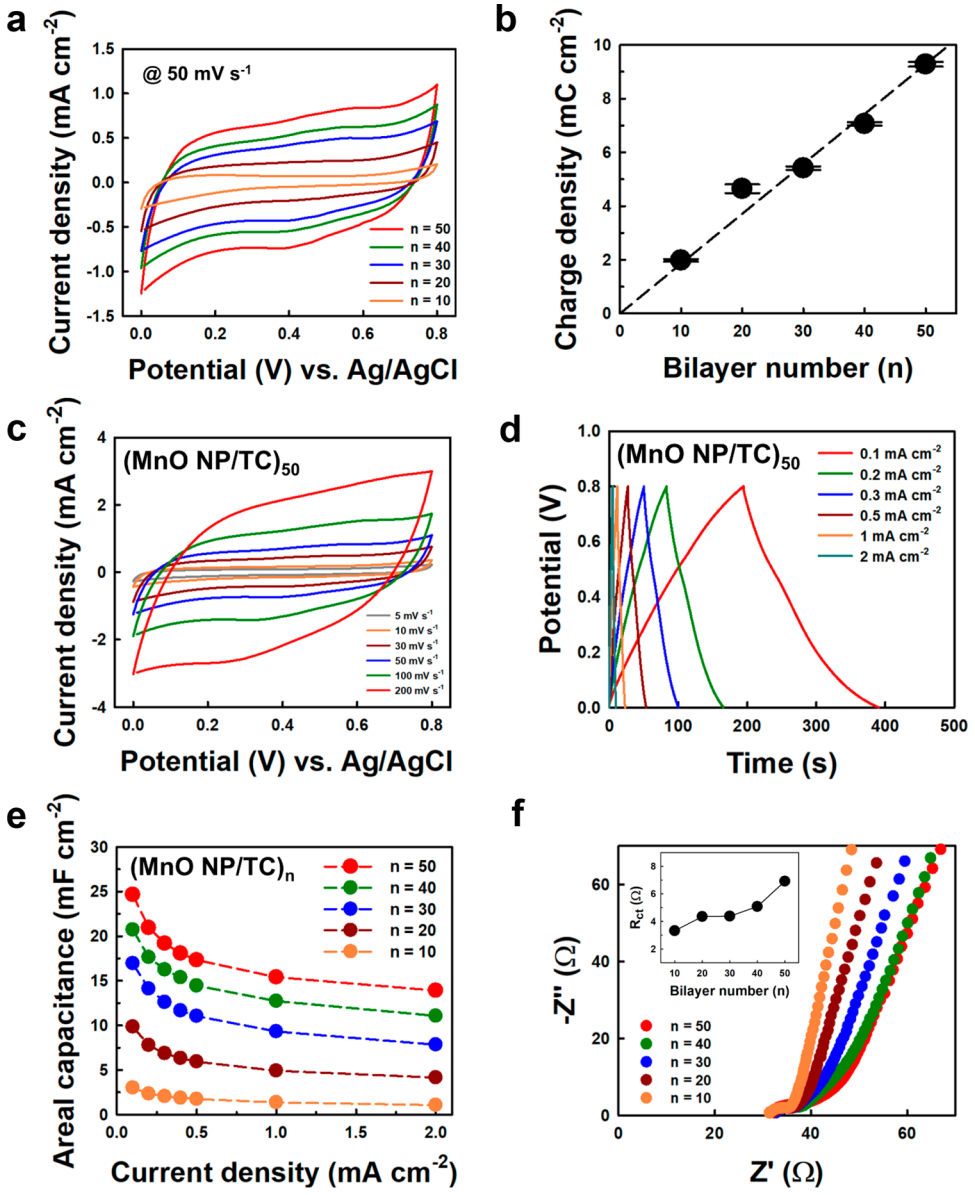

Figure 2. (a) CV curves and (b) the total integrated charge density of the $(MnO\ NP/TC)_n$ electrodes at a scan rate of 50 mV s^{-1} as a function of the bilayer number (n). (c) Scan-rate-dependent CVs of the $(MnO\ NP/TC)_{50}$ electrode measured at 5−200 mV s^{-1}. (d) GCD curves of the $(MnO\ NP/TC)_{50}$ electrode at various current densities in the range of 0.1−2 mA cm^{-2}. (e) Areal capacitances of the $(MnO\ NP/TC)_n$ electrodes with increasing current density from 0.1 to 2 mA cm^{-2}. (f) Nyquist plots and charge transfer resistances (R_{ct}; inset) of the $(MnO\ NP/TC)_n$ electrodes as a function of bilayer number (n).

was determined to be ~87.7% by thermogravimetric analysis (TGA) (Figure S2). Such a high ratio indicates that the ligand exchange-based LbL approach can maximize the loading amount of energy storage components within ultrathin films by minimizing the use of electrochemically inactive materials (*i.e.*, insulating organic ligands or linkers). As the bilayer number (n) of the $(MnO\ NP/TC)_n$ multilayers increased from 10 to 50, the film thickness was linearly increased from 81 to 410 nm (Figure 1d). We also confirmed that the $(MnO\ NP/TC)_n$ multilayers can be assembled uniformly on the ITO glass (Figure S3). Additionally, the root-mean-square (rms) surface roughness of the $(MnO\ NP/TC)_{50}$ multilayers measured from atomic force microscopy (AFM) was 4.19 nm (Figure 1e and Figure S4). Notably, this low surface roughness of the multilayers has no significant effect on their light scattering, and Figure 1f shows optical transmittance spectra and optical images of $(MnO\ NP/TC)_n$ multilayer-coated ITO glasses as a function of bilayer number (n). When the bilayer number was increased from n = 10 to 50, the optical transmittance of the multilayers measured at a wavelength of 550 nm gradually decreased from 86% to 62% due to the slight light absorbance of MnO NPs in the given wavelength range (Figure S5).

On the basis of these results, we explored the possibility that $(MnO\ NP/TC)_n$ multilayers could be effectively used as an ultrathin TSC electrode. For this investigation, the charge storage performance of the $(MnO\ NP/TC)_n$ multilayers deposited onto an ITO substrate (*i.e.*, $(MnO\ NP/TC)_n$ electrodes) was evaluated using cyclic voltammetry (CV) and galvanostatic charge/discharge (GCD) measurements in a three-electrode cell configuration using 0.5 M Na_2SO_4 as an electrolyte. First, CV scans of the $(MnO\ NP/TC)_n$ electrodes were measured as a function of the bilayer number (n) in a

DOI: 10.1021/acsnano.9b04594
ACS Nano 2019, 13, 12719−12731

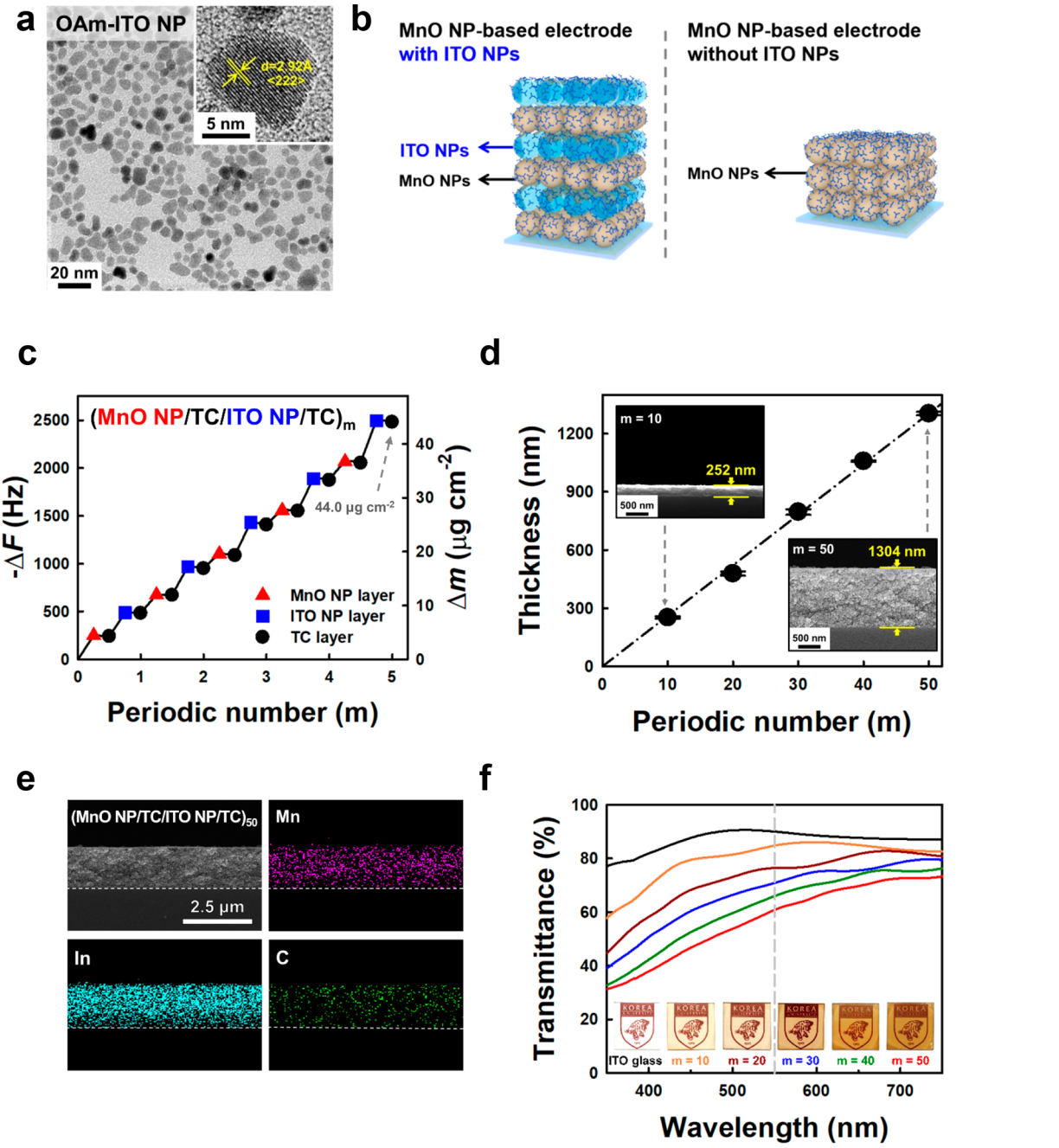

Figure 3. (a) HR-TEM images of synthesized OAm-ITO NPs. (b) Schematic illustration of MnO NP-based TSC electrodes with the conductive/transparent ITO NPs. (c) Frequency and mass change of $(MnO\ NP/TC/ITO\ NP/TC)_m$ multilayers as a function of the periodic number (m). (d) Thickness change of $(MnO\ NP/TC/ITO\ NP/TC)_m$ multilayers measured from the cross-sectional FE-SEM images (insets). (e) EDS mapping images of a $(MnO\ NP/TC/ITO\ NP/TC)_{50}$ multilayer. (f) Transmittance spectra and digital images of the $(MnO\ NP/TC/ITO\ NP/TC)_m$ multilayers on ITO glass with increasing periodic number (m). The university logos were used with permission from Korea University.

potential window of 0−0.8 V *vs* Ag/AgCl at a scan rate of 50 mV s^{-1} (Figure 2a). In the CV curves, the broad redox peaks between the different states of the Mn ions were observed around 0.55 V (anodic peak) and at 0.45 V (cathodic peak).[48] These peaks indicate that the Mn ions are reduced and oxidized between Mn(II) and Mn(III), as in the Pourbaix diagram of Mn ions.[49] Therefore, the mechanism of energy storage of manganese oxides in an aqueous solution can be expressed and simplified as follows:[50]

$$MnO + xC^+ + yH^+ + (x + y)e^- \leftrightarrow MnOC_xH_y \quad (1)$$

$$Mn(II) \leftrightarrow Mn(III) + e^- \quad (2)$$

Moreover, the current level of the quasi-rectangular CV scans was observed to increase with increasing bilayer number (or multilayer thickness), and the total charge density calculated from the integrated area of the CV scans increased almost linearly with the bilayer number of the multilayer electrodes (Figure 2b). This linear trend implies that the capacity of the electrodes can be further enhanced and exactly controlled by adjusting the bilayer number. The rate capability of the $(MnO\ NP/TC)_{50}$ electrode was also evaluated from CV

DOI: 10.1021/acsnano.9b04594
ACS Nano 2019, 13, 12719−12731

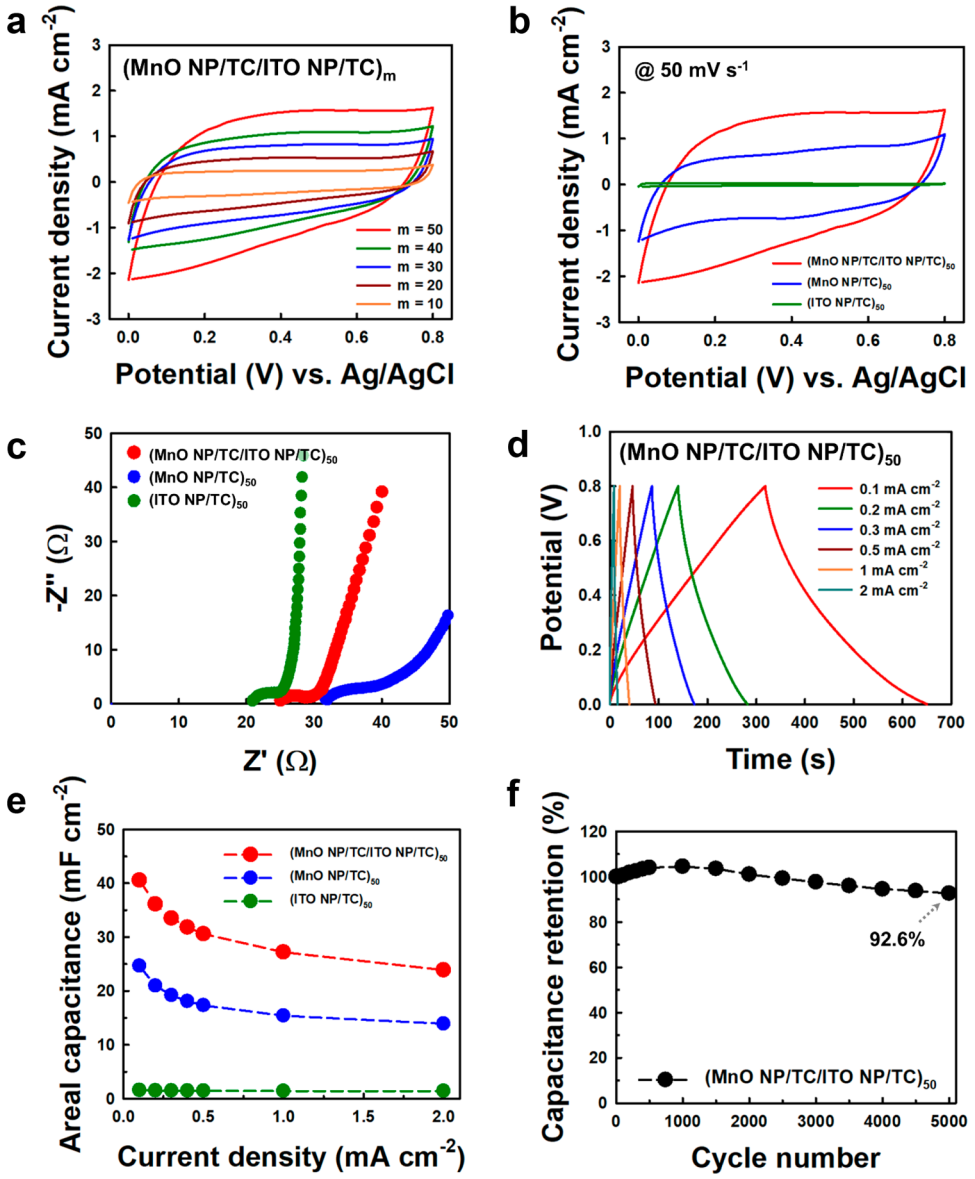

Figure 4. (a) CV curves of the $(MnO\ NP/TC/ITO\ NP/TC)_m$ electrode as a function of the periodic number (m) at a scan rate of 50 mV s^{-1}. (b) Comparison of CV scans among the $(MnO\ NP/TC/ITO\ NP/TC)_{50}$, $(MnO\ NP/TC)_{50}$, and $(ITO\ NP/TC)_{50}$ electrodes in 0.5 M Na_2SO_4 at a scan rate of 50 mV s^{-1}. (c) Nyquist plots of the $(MnO\ NP/TC/ITO\ NP/TC)_{50}$, $(MnO\ NP/TC)_{50}$, and $(ITO\ NP/TC)_{50}$ electrodes. (d) GCD curves of the $(MnO\ NP/TC/ITO\ NP/TC)_{50}$ electrode at various current densities in the range of 0.1−2 mA cm^{-2}. (e) Comparison of areal capacitances among the $(MnO\ NP/TC/ITO\ NP/TC)_{50}$, $(MnO\ NP/TC)_{50}$, and $(ITO\ NP/TC)_{50}$ electrodes. (f) Cycling retention of the $(MnO\ NP/TC/ITO\ NP/TC)_{50}$ electrode during GCD measurements at 2 mA cm^{-2}.

scans with scan rates varied from 5 to 200 mV s^{-1} (Figure 2c) and from GCD curves with various current densities ranging from 0.1 to 2 mA cm^{-2} (Figure 2d). The $(MnO\ NP/TC)_{50}$ electrode with a thickness of ∼410 nm exhibited a high areal capacitance of 24.6 mF cm^{-2} at a low current density of 0.1 mA cm^{-2} and maintained its high capacitance of ∼13.9 mF cm^{-2} at a high current density of 2.0 mA cm^{-2} (Figure 2e and Figure S6). These results imply that the multilayer electrodes have good rate capability due to the relatively facile charge transfer through the densely packed but ultrathin MnO NP arrays. To investigate the charge transfer characteristics of the $(MnO\ NP/TC)_n$ electrodes, electrochemical impedance spectroscopy (EIS) measurements were further conducted in the frequency range from 100 kHz to 0.1 Hz at a potential amplitude of 5 mV (Figure 2f). The charge transfer resistance (*i.e.*, R_{ct}, which is related to the charge transfer at the electrode−electrolyte interface) of the multilayer electrodes was slightly increased from approximately 3.3 Ω to 6.9 Ω with increasing bilayer number from 10 to 50. Additionally, when the bilayer number (or film thickness) is increased, the slope of the straight tail in the low-frequency region (Warburg impedance) slightly decreased due to the increase in the ion diffusion resistance.

Although the charge transfer and ion diffusion resistances of the electrodes were increased with increasing the loading amount of active materials, the electrochemical performance of the $(MnO\ NP/TC)_n$ electrodes was notably improved compared to that of other conventional LbL-assembled electrodes using polymer linkers. As a control sample, LbL-assembled electrodes were prepared by alternatively depositing MnO NPs and bulky poly(acrylic acid) (PAA, $M_w \approx 1800$) instead of TC, generating $(MnO\ NP/PAA)_n$ multilayers. The

DOI: 10.1021/acsnano.9b04594
ACS Nano 2019, 13, 12719−12731

assembled $(MnO\ NP/PAA)_{50}$ electrode exhibited worse electrochemical performance than that of the $(MnO\ NP/TC)_{50}$ electrode (Figure S7a,b). This poor performance of the $(MnO\ NP/PAA)_{50}$ electrode can be attributed to the increased charge transfer resistance ($R_{ct} \approx 68\ \Omega$) compared to that of the $(MnO\ NP/TC)_{50}$ electrode ($R_{ct} \approx 6.9\ \Omega$) (Figure S7c). Therefore, it is reasonable to conclude that the $(MnO\ NP/TC)_n$ multilayers with minimized separation distance can reduce the charge transport length scale compared to that of $(MnO\ NP/PAA)_n$ multilayers using polymer linkers, resulting in improved electrochemical performance.

Moreover, we tried to further enhance the energy storage performance of the electrodes by reducing the internal resistance of the transparent electrodes. Although other research groups also reported that the insertion of conductive materials such as Au NPs or carbon-based materials into the electrode could promote the capacitance through reducing internal resistance,[51,52] it should be noted that the used conductive materials had a strong light absorption property, adversely affecting optical transparency. Therefore, we focused on lowering the internal resistance of TSCs without a meaningful loss of optical transparency. This task consists of finding an approach to address the complex trade-off between areal capacitance and optical transmittance as well as that between areal capacitance and rate capability. For this purpose, conductive and transparent OAm-ITO NPs with a diameter of approximately 7 ± 2 nm and high crystallinity were prepared in toluene (Figure 3a) and then were periodically inserted into $(MnO\ NP/TC)_n$ multilayers using the above-mentioned ligand exchange-based LbL assembly method (Figure 3b). In this case, it was expected that the incorporated ITO NPs could provide beneficial electron transfer pathways (by reducing the charge transfer resistance) within the MnO NP-based electrodes with negligible loss of optical transmittance. First, we investigated the adsorption behavior and mechanism of $(ITO\ NP/TC)_n$ multilayers. As mentioned previously, the OAm ligands bound to the surface of ITO NPs could be replaced by the multidentate TC linkers during LbL deposition (Figure S8). Similar to the $(MnO\ NP/TC)_n$ multilayers, the $(ITO\ NP/TC)_n$ multilayers exhibited regular growth, a uniform thickness increase, a high mass ratio of the embedded ITO NPs, and transparent optical properties, as confirmed by QCM, cross-sectional field emission scanning electron microscopy (FE-SEM) images, TGA, and UV−vis spectroscopy measurements, respectively (Figure S9). Interestingly, the assembled $(ITO\ NP/TC)_n$ multilayers showed considerably higher charge storage capability than the bulk ITO film. When a 168-nm-thick $(ITO\ NP/TC)_{12}$ multilayer was deposited onto 166-nm-thick ITO-coated glass (*i.e.*, bare ITO glass), the CV current level of the ITO NP-based electrode was significantly higher than that of bare ITO glass (Figure S10a). This higher electrochemical performance of ITO NP-based multilayers than bulk ITO glass was mainly due to the large specific surface area of the ITO NPs. Furthermore, the $(ITO\ NP/TC)_{50}$ electrode displayed nearly rectangular CV curves and triangular GCD curves originating from its double-layer capacitive behavior and good rate capability (Figure S10b,c). The ITO NP-based electrode retained 98.5% of its initial capacitance even after 10 000 GCD cycles, demonstrating excellent stability (Figure S10d).

Motivated by these results, we regularly deposited $(MnO\ NP/TC/ITO\ NP/TC)_m$ multilayers onto the substrates, inducing a greater thickness (or total loading amount) than that of the ITO NP-free $(MnO\ NP/TC)_n$ multilayers with the same layer number of MnO NPs (Figure 3c,d). Moreover, as shown in energy dispersive X-ray spectroscopy (EDS) images (Figure 3e and Figure S11), the inserted ITO NPs were uniformly and densely distributed within the multilayer films with a high mass ratio of NPs (~92.8%) (Figure S12a). The rms surface roughness of the $(MnO\ NP/TC/ITO\ NP/TC)_{50}$ multilayers was estimated to be 4.52 nm, which was similar to that of the $(MnO\ NP/TC)_{50}$ multilayers (~4.19 nm) (Figure S12b). A striking feature of these ITO NP-incorporated multilayers is that the optical transmittance of the $(MnO\ NP/TC/ITO\ NP/TC)_m$ electrodes is fairly similar to that of the $(MnO\ NP/TC)_n$ electrodes with the same layer number of MnO NPs despite the substantial increase in total thickness due to the periodic insertion of ITO NPs (Figure 3f). Specifically, the optical transmittance values of the 1304-nm-thick $(MnO\ NP/TC/ITO\ NP/TC)_{50}$ and 410-nm-thick $(MnO\ NP/TC)_{50}$ multilayers were 60.8% and 61.6% at 550 nm, respectively.

The charge storage capability of the $(MnO\ NP/TC/ITO\ NP/TC)_m$ electrodes was investigated using CV scans as a function of the periodic layer number (m) at a scan rate of 50 mV s^{-1} (Figure 4a). The current levels of the quasi-rectangular-type CV scans increased as the periodic layer number increased, and the scan-rate-dependent CV scans showed the rapid capacitive behavior of the ITO NP-incorporated MnO NP electrodes (Figure S13). In particular, the superior electrochemical performance of ITO NP-inserted electrodes can be made more evident by the comparison among three different kinds of electrodes (*i.e.*, the $(ITO\ NP/TC)_{50}$, $(MnO\ NP/TC)_{50}$, and $(MnO\ NP/TC/ITO\ NP/TC)_{50}$ electrodes) (Figure 4b). The total charge densities calculated from the integrated area of the CV scans of the $(ITO\ NP/TC)_{50}$, $(MnO\ NP/TC)_{50}$, and $(MnO\ NP/TC/ITO\ NP/TC)_{50}$ electrodes at a scan rate of 50 mV s^{-1} were approximately 0.36, 9.28, and 17.7 mC cm^{-2}, respectively. Given that the double-layer capacitance of the inserted ITO NPs is much smaller than the pseudocapacitance of the MnO NPs, this notable increase in the charge density of the $(MnO\ NP/TC/ITO\ NP/TC)_{50}$ electrode implies that the periodically inserted ITO NP layers can significantly reduce the internal resistance and consequently facilitate charge transfer. These possible explanations were also confirmed by EIS measurement (Figure 4c). Although the equivalent series resistance (ESR) and R_{ct} values of the ITO NP-incorporated electrodes (*i.e.*, ESR and R_{ct} of $(MnO\ NP/TC/ITO\ NP/TC)_{50} \approx 25.2$ and $5.3\ \Omega$, respectively) were higher than those of the $(ITO\ NP/TC)_{50}$ electrodes (ESR and R_{ct} of $(ITO\ NP/TC)_{50}$ ~21 and $4.3\ \Omega$, respectively), these values were much lower than those of the $(MnO\ NP/TC)_{50}$ electrode (ESR and R_{ct} of $(MnO\ NP/TC)_{50} \approx 32$ and $6.9\ \Omega$, respectively) despite the increased electrode thickness. These results clearly show that the periodically incorporated ITO NPs facilitate electron transfer between neighboring PC NPs with poor electrical conductivity. In Bode plots, it was confirmed that the phase angle of the ITO-inserted electrode in the low-frequency region was closer to −90° than that of the ITO NP-free electrode, indicating the better ideal capacitor behavior (Figure S14). However, in a high-frequency region, the peak denoted by φ was slightly shifted to a lower frequency region by the inserted ITO NPs, suggesting an increase of the diffusive resistance of ions.[53,54] The increased ion diffusive resistance can be caused by an increase in the total thickness of the multilayer due to the

DOI: 10.1021/acsnano.9b04594
ACS Nano 2019, 13, 12719−12731

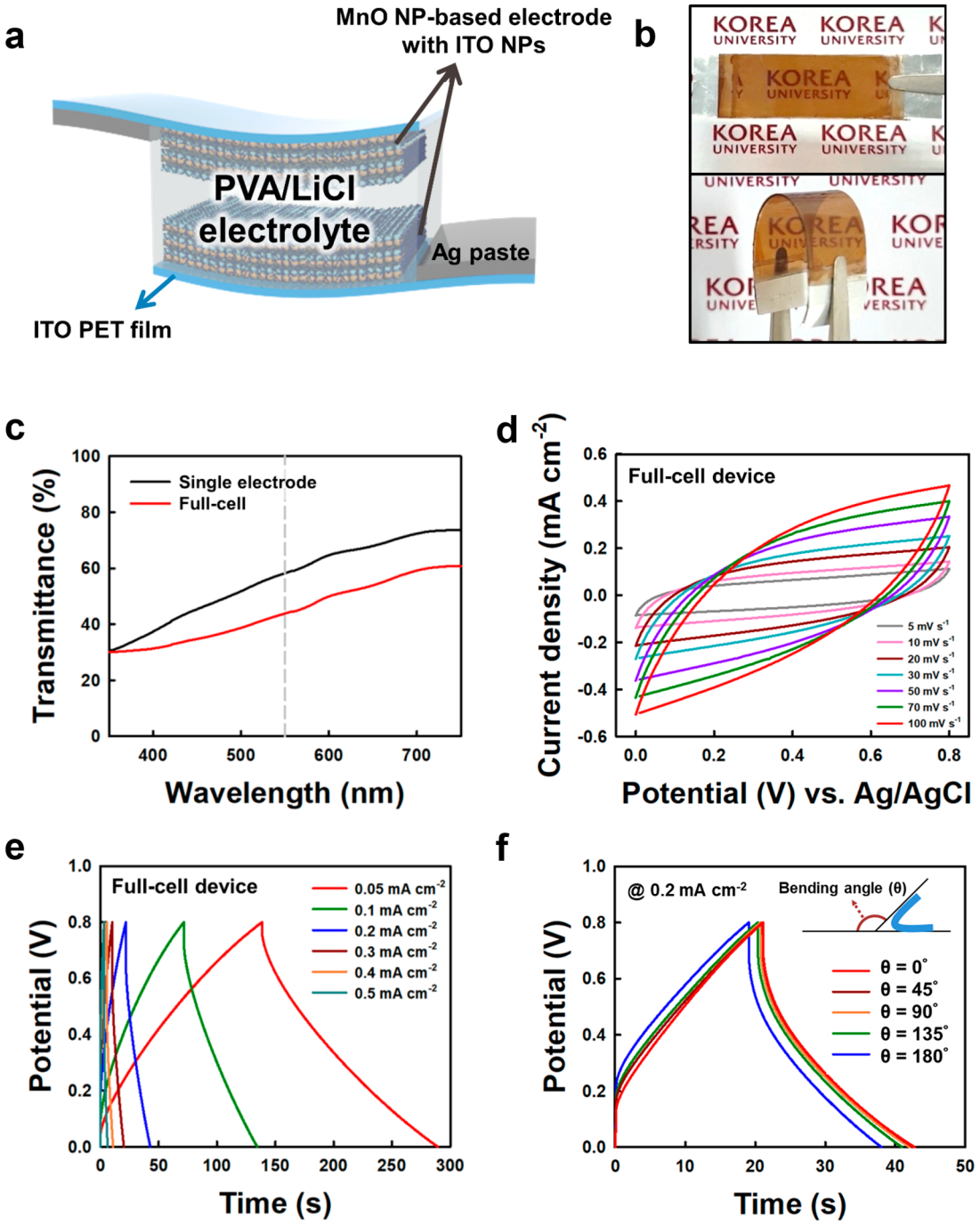

Figure 5. (a) Schematic illustration and (b) photographic images of a flexible and symmetric solid-state TSC. The university logos were used with permission from Korea University. (c) Transmittance spectra of the single electrode and the full-cell TSC device. (d) CV curves of the full-cell TSC device as a function of scan rate. (e) GCD curves of the full-cell TSC device as a function of current density. (f) GCD curves of the full-cell TSC device according to the bending angle at a current density of 0.2 mA cm^{-2}.

insertion of ITO NPs. However, considering that the electrochemical performance of electrodes was significantly improved by the incorporated-ITO NPs, it is reasonable to conclude that the enhanced electrical conductivity (*i.e.*, the reduced R_{ct}) is a dominant factor contributing to the capacitive behavior.

The areal capacitance of the $(MnO\ NP/TC/ITO\ NP/TC)_m$ electrodes was evaluated as a function of the periodic layer number (m) using GCD curves acquired at varied current densities ranging from 0.1 to 2 mA cm^{-2} (Figure 4d and Figure S15). Their GCD curves displayed the typical triangular feature, implying the good capacitive behavior of the ITO NP-incorporated MnO NP electrodes. The areal capacitances of the $(MnO\ NP/TC/ITO\ NP/TC)_m$ electrodes gradually increased with increasing periodic layer number (m) from 10 to 50 (Figure S16). It should particularly be noted that the energy storage performance of the $(MnO\ NP/TC/ITO\ NP/TC)_{50}$ electrode was superior to that of the $(MnO\ NP/TC)_{50}$ electrode over the entire current density range (Figure 4e). The maximum areal capacitance of the $(MnO\ NP/TC/ITO\ NP/TC)_{50}$ electrode was calculated to be approximately 41 mF cm^{-2} (at 0.1 mA cm^{-2}), which was 1.6 times higher than that

DOI: 10.1021/acsnano.9b04594
ACS Nano 2019, 13, 12719−12731

of the $(MnO\ NP/TC)_{50}$ electrode (24.6 mF cm^{-2} at 0.1 mA cm^{-2}). In addition, the $(MnO\ NP/TC/ITO\ NP/TC)_{10}$ electrode also exhibited a high areal performance of 8.45 mF cm^{-2} at 0.1 mA cm^{-2} despite its high optical transmittance of 84.7%. Furthermore, we investigated the cycling stability of the $(MnO\ NP/TC/ITO\ NP/TC)_{50}$ electrode at 2 mA cm^{-2}. In this case, the ITO NP-incorporated electrode retained 92.6% of its initial capacitance after 5000 GCD cycles (Figure 4f), indicating that the $(MnO\ NP/TC/ITO\ NP/TC)_{50}$ electrode was highly stable despite the use of a small organic linker. Additionally, the slight increase in capacitance during the initial cycling test (*i.e.*, the initial 500 cycles) may be attributable to the increase in the effective interfacial area between the electrode and electrolyte, as well as surface activation of the electrode materials during electrochemical cycling.[55,56] As shown in Figure S17, the self-discharge characteristics of the $(MnO\ NP/TC/ITO\ NP/TC)_{50}$ electrode were investigated after charging the electrode in 0.8 V. In this case, the time-dependent voltage drop was observed at open-circuit voltage. This self-discharge process relatively rapidly occurred during the first 1 h, and then the potential drop was slowly decreased. Particularly, when we plotted the data against the logarithm of time, the self-discharge profile exhibited a linear drop after a plateau, as shown in Figure S17b. This observation indicates the activation-controlled Faradaic reaction with charge redistribution.[57,58] These results evidently demonstrate that the elaborate interface design through the insertion of conductive ITO NPs as well as the ligand replacement of bulky native ligands (*i.e.*, OA, OAm, and/or OCA) with small-molecule TC linkers allows decreased charge transfer resistance, easier penetration of the electrolyte, improved utilization of active materials, and more stable electrochemical operation.

On the basis of these results, we prepared a flexible and symmetric TSC (FS-TSC) composed of positive and negative $(MnO\ NP/TC/ITO\ NP/TC)_{50}$ electrodes that were deposited onto ITO-coated PET substrates (Figure S18). The preparation methods, multilayer structures, and electrochemical properties of the FS-TSCs exactly coincided with those of the above-mentioned ITO-incorporated MnO NP electrodes (for a single electrode) (Experimental Section and Figure 5a). First, the letters ("KOREA University") printed under the solid-state FS-TSC were clearly visible with the naked eye, and the specific optical transmittance of the FS-TSC was measured to be approximately 44% at a wavelength of 550 nm (for comparison, the transmittance of a single electrode is ~58.2% at 550 nm) (Figure 5b,c). Notably, merely decreasing the periodic layer number (m) increases the optical transparency. The electrochemical performance of the solid-state FS-TSC device was assessed in a voltage window of 0.8 V with a solid poly(vinyl alcohol) (PVA)/LiCl electrolyte. In this case, the quasi-rectangular CV curves and the symmetric triangular GCD curves of the solid-state FS-TSC device at various rates (*i.e.*, different voltages ranging from 5 to 100 mV s^{-1} and varied current densities from 0.05 to 0.5 mA cm^{-2}) revealed its desirable capacitive feature and excellent rate capability despite the use of a solid-state electrolyte as well as the increase in the total electrode thickness (Figure 5d,e). The areal capacitances of the FS-TSC (calculated from the GCD profiles) at current densities of 0.05 and 0.5 mA cm^{-2} were calculated to be approximately 10.1 and 3.42 mF cm^{-2}, respectively. Furthermore, the maximum areal power and energy density of this device were measured to be approximately 113 μW cm^{-2} and 0.82 μWh cm^{-2}, respectively, which were much superior to those of most other TSCs.[11,20−22,59,60] In addition, the device exhibited a 76% cycling retention after 5000 GCD cycles at 0.5 mA cm^{-2}, confirming the operational stability of the device (Figure S19). Lastly, the electrochemical performance of the FS-TSC device was also investigated under various bending angles, as shown in Figure 5f. When the device was bent from 0° to 180°, there was no notable difference in the GCD curves. Specifically, the areal capacitance maintained 90% of the initial capacitance (9.1 mF cm^{-2} at 0.05 mA cm^{-2}) (Figure S20). In addition, as shown in Figure S21, the transmittance of the device remained stable without any significant change even after the cycling test and the bending test. Notably, the mechanical flexibility and conductivity of ITO-coated PET film substrates can also have significant effects on the device performance depending on the bending angle (or degree of flexibility). Therefore, the mechanical stimuli-induced energy storage performance of FS-TSCs can be further improved with other types of flexible current collectors. Finally, the CV and GCD profiles of two, three, and four cells connected in series and parallel were measured for practical applications (Figure S22). The voltage window was enlarged linearly with increasing the number of cells connected in series. In the case of parallel connection, the capacitance was increased according to the number of cells. As shown in the digital image of Figure S22e, three cells connected in series could operate a red LED (2.1 V), demonstrating the possibility of applying the LbL-assembled TSCs to the transparent electronics.

CONCLUSION

We demonstrated that high-performance TSCs (including a solid-state FS-TSC) with high areal capacitance, excellent rate capability, and good optical transmittance could be prepared using the alternating LbL assembly between high-energy MnO NP and ITO NP arrays without unnecessary bulky organics or electrochemically inactive components. Through a ligand exchange reaction during LbL deposition, the TC molecular linker serving as a ligand directly bridged all the interfaces between neighboring NPs, which can minimize the NP−NP separation distance. Moreover, the periodic insertion of conductive/transparent ITO NPs within MnO NP-based electrodes significantly reduced the charge transfer resistance of the electrodes without a notable loss of optical transmittance, resulting in high electrochemical performance and good transparency. Another feature of our approach is that the electrochemical performance and optical transparency of LbL-assembled TSCs can be easily but exactly controlled by the number of deposition layers of MnO and/or ITO NPs. As a result, we highlight that our approach can innovatively mitigate the troublesome trade-off between areal capacitance and optical transmittance as well as that between areal capacitance and rate capability. Finally, we believe that the introduced LbL approach can provide an important basis for designing a variety of electrochemical applications requiring low charge transfer resistance.

EXPERIMENTAL SECTION

Synthesis of OA-MnO NPs. OA-MnO NPs with a diameter of 10 nm in toluene were prepared as previously reported.[61] First, manganese(II) chloride tetrahydrate ($MnCl_2{\cdot}4H_2O$, 40 mmol, Sigma-Aldrich) and sodium oleate (80 mmol, TCI Co., Ltd.) were added to a solution composed of ethanol (30 mL), *n*-hexane (70 mL),

DOI: 10.1021/acsnano.9b04594
ACS Nano 2019, 13, 12719−12731

and deionized water (40 mL), and then the mixture was stirred at 70 °C for 12 h under an argon atmosphere. The Mn-oleate complex formed in the organic solvent was separated from the water phase and then evaporated to obtain a complex powder. For the synthesis of OA-MnO NPs, the Mn oleate powder (1.24 g) was mixed with 1-hexadecene (12.8 mL) at 70 °C for 1 h. The mixture was gradually heated to 280 °C at a heating rate of 1.9 °C min^{-1} under argon gas and then maintained at 280 °C for 10 min. After the isothermal process, the resultant solution was slowly cooled and then rinsed by centrifugation. The obtained hydrophobic OA-MnO NPs were redispersed in a nonpolar solvent such as toluene.

Synthesis OAm-ITO NPs. All chemicals used in the synthesis of OAm/OCA-stabilized ITO NPs (OAm-ITO NPs) were purchased from Sigma-Aldrich. OAm-ITO NPs with a diameter of approximately 7 nm were prepared in toluene using a method reported by Kanehara *et al.*[62] Briefly, indium(III) acetate (1.08 mmol) and tin(II) 2-ethylhexanoate (0.12 mmol) were added to a dioctyl ether (10 mL) solution containing *n*-octanoic acid (3.6 mmol) and OAm (30 mmol), and then the reaction mixture was stirred at 80 °C for 30 min. After the mild heating process, the mixture was heated at 150 °C for 1 h under an argon atmosphere, and then it was heated again at 280 °C for 2 h. After these successive heating processes, the reaction mixture was slowly cooled to room temperature and then purified with excess acetone using centrifugation several times. The obtained OAm-ITO NPs were dispersed in toluene.

Preparation of LbL-Assembled Multilayers. For the preparation of LbL-assembled $(MnO\ NP/TC)_n$, $(MnO\ NP/TC)_n$, and $(MnO\ NP/TC/ITO\ NP/TC)_m$ multilayers, the surfaces of Si wafers, quartz glasses (for UV−vis absorbance analysis), gold-sputtered Si wafers (for FTIR spectroscopy analysis), QCM electrodes (for loading amount analysis), and 160-nm-thick ITO-coated glass with a sheet resistance of 20 Ω sq^{-1} (for electrochemical analysis) were treated by irradiation with UV light ($\lambda \approx 350$ nm) for 30 min. First, a poly(ethyleneimine) (PEI) solution in ethanol (1 mg mL^{-1}, $M_w \approx 800$) was deposited onto the substrates using spin-coating at 3000 rpm for 15 s, and then the PEI-coated substrates were thoroughly rinsed twice by the spin-coating of pure ethanol. Next, a 10 mg mL^{-1} OA-MnO NP solution (or OAm-ITO NP solution) was deposited onto the PEI-coated substrates with the same procedure and then washed with pure toluene twice to remove the weakly absorbed OA-MnO NPs. Subsequently, TC in ethanol (2 mg mL^{-1}) was deposited onto the outermost OA-MnO NP layer-coated substrate and then washed with pure ethanol twice. These deposition cycles were repeated until the desired bilayer number was reached. The $(ITO\ NP/TC)_n$ or $(MnO\ NP/TC/ITO\ NP/TC)_m$ multilayers were also prepared through the same procedure with the same solution concentrations.

Preparation of Flexible and Symmetric Solid-State Supercapacitor. For the preparation of flexible and symmetric solid-state supercapacitors composed of positive and negative $(MnO\ NP/TC/ITO\ NP/TC)_{50}$ electrodes, these LbL-assembled multilayers were deposited onto flexible ITO-coated poly(ethylene terephthalate) (PET) substrates. In this case, a PVA/LiCl gel electrolyte was prepared by dissolving PVA (1 g) and 1 g of LiCl in 10 mL of deionized water with continuous stirring at 85 °C for 1 h. After the PVA/LiCl gel became clear, the electrolyte gel was coated on the electrode with an effective working area of 1 cm^2 and dried at room temperature until the gel solidified. Finally, a flexible solid-state supercapacitor device was fabricated by assembling two electrodes together.

Characterization. The crystal structure and size distribution of OA-MnO NPs and OAm-ITO NPs were investigated by HR-TEM (Tecnai 20, FEI). The crystallinity of OAm-ITO NPs was also examined through an X-ray diffraction pattern obtained from a SmartLab (Rigaku) with Cu Kα radiation. To confirm the ligand exchange reaction-based adsorption mechanism, FTIR spectra of the LbL-assembled multilayer films was measured with a Cary 600 spectrometer (Agilent Technology) operated in ATR mode with a 4 cm^{-1} resolution. The measured data were analyzed using spectrum analysis software (Omnic 9, Thermo Scientific). The vertical growth and optical transmittance of multilayers were monitored by a UV−vis spectrophotometer (Lambda 35, PerkinElmer) in a scan range from 200 to 1000 nm. Additionally, the film growth was quantitatively measured using a QCM (QCM 200, SRS). The mass change (Δm) of multilayers was calculated from the changes in the frequency (ΔF) using the Sauerbrey equation,[63] eq 3:

$$\Delta F\ (\mathrm{Hz}) = -56.6 \times \Delta m_A \tag{3}$$

where Δm_A is the mass change per quartz crystal unit area in $\mu g\ cm^{-2}$. The film thickness and EDX images of multilayers were observed through FE-SEM (Quanta 250 FEG, FEI). The mass ratio of metal oxide components within LbL-assembled multilayers was analyzed by TGA (Q50, TA Instruments).

Electrochemical Measurements. All the electrochemical measurements were conducted with an Ivium-n-Stat electrochemical workstation (Ivium Technologies). A three-electrode system was applied to test the electrochemical performance of a single electrode, and a two-electrode cell system was applied to evaluate the performance of the solid-state supercapacitor. In the three-electrode system composed of a Ag/AgCl reference electrode, a Pt counter electrode, and a working electrode, the electrochemical properties of the working electrodes (*i.e.*, MnO NP-based multilayer electrodes with ITO NPs and without ITO NPs, active area ~1 cm^2) were investigated in a 0.5 M Na_2SO_4 electrolyte. For the flexible and symmetric solid-state supercapacitors, PVA/LiCl gels were used as both the separator and electrolyte. CV and GCD were measured in a potential range from 0 to +0.8 V. EIS measurements were performed over the frequency range from 100 kHz to 0.1 Hz at a potential amplitude of 5 mV. In this case, the areal capacitance (C) was calculated from the GCD curves using the following eq 4:

$$C = \frac{I\Delta t}{\Delta V} \tag{4}$$

where I is the discharge current density, Δt is the discharge time, and ΔV is the operating voltage window. In addition, the energy (E) and power (P) density were calculated from the GCD profiles as follows:[64]

$$E = \frac{C\Delta V^2}{7200} \tag{5}$$

$$P = \frac{E \times 3600}{\Delta t} \tag{6}$$

ASSOCIATED CONTENT

Supporting Information

The Supporting Information is available free of charge on the ACS Publications website at DOI: 10.1021/acsnano.9b04594.

FTIR spectra of pristine OA-MnO NPs and TC; TGA profile, AFM images and surface roughness profiles, UV−vis spectra, and GCD profiles of $(MnO\ NP/TC)_n$ multilayers; electrochemical performances of $(MnO\ NP/PAA)_n$ multilayers; FTIR spectra, QCM measurement, thickness change, TGA profile, UV−vis spectra, and CV curves of $(ITO\ NP/TC)_n$ multilayers; TGA profile, AFM image, surface roughness profile, and electrochemical performances of $(MnO\ NP/TC/ITO\ NP/TC)_m$ multilayers (PDF)

AUTHOR INFORMATION

Corresponding Authors

*seung.lee@me.gatech.edu.

*jinhan71@korea.ac.kr.

ORCID

Jimin Choi: 0000-0001-6787-3058

Cheong Hoon Kwon: 0000-0002-9516-0669

DOI: 10.1021/acsnano.9b04594
ACS Nano 2019, 13, 12719−12731

Jinhan Cho: 0000-0002-7097-5968

Notes

The authors declare no competing financial interest.

ACKNOWLEDGMENTS

This work was supported by a National Research Foundation (NRF) of Korea grant funded by the Ministry of Science, ICT & Future Planning (MSIP) (NRF-2018R1A2A1A05019452; NRF-2019R1A4A1027627) and the Basic Science Research Program through the National Research Foundation (NRF) of Korea funded by the Ministry of Education (NRF-2017R1A6A3A04003192).

REFERENCES

(1) Nomura, K.; Ohta, H.; Ueda, K.; Kamiya, T.; Hirano, M.; Hosono, H. Thin-Film Transistor Fabricated in Single-Crystalline Transparent Oxide Semiconductor. *Science* **2003**, *300*, 1269−1272.

(2) Lipomi, D. J.; Vosgueritchian, M.; Tee, B. C.; Hellstrom, S. L.; Lee, J. A.; Fox, C. H.; Bao, Z. Skin-Like Pressure and Strain Sensors Based on Transparent Elastic Films of Carbon Nanotubes. *Nat. Nanotechnol.* **2011**, *6*, 788−792.

(3) Hosseini, P.; Wright, C. D.; Bhaskaran, H. An Optoelectronic Framework Enabled by Low-Dimensional Phase-Change Films. *Nature* **2014**, *511*, 206−211.

(4) Salvatore, G. A.; Munzenrieder, N.; Kinkeldei, T.; Petti, L.; Zysset, C.; Strebel, I.; Buthe, L.; Troster, G. Wafer-Scale Design of Lightweight and Transparent Electronics That Wraps Around Hairs. *Nat. Commun.* **2014**, *5*, 2982.

(5) Kim, C.-C.; Lee, H.-H.; Oh, K. H.; Sun, J.-Y. Highly Stretchable, Transparent Ionic Touch Panel. *Science* **2016**, *353*, 682−687.

(6) An, B. W.; Heo, S.; Ji, S.; Bien, F.; Park, J.-U. Transparent and Flexible Fingerprint Sensor Array with Multiplexed Detection of Tactile Pressure and Skin Temperature. *Nat. Commun.* **2018**, *9*, 2458.

(7) Kim, K. S.; Zhao, Y.; Jang, H.; Lee, S. Y.; Kim, J. M.; Kim, K. S.; Ahn, J. H.; Kim, P.; Choi, J. Y.; Hong, B. H. Large-Scale Pattern Growth of Graphene Films for Stretchable Transparent Electrodes. *Nature* **2009**, *457*, 706−710.

(8) Hsu, C. W.; Zhen, B.; Qiu, W.; Shapira, O.; DeLacy, B. G.; Joannopoulos, J. D.; SoljaČiĆ, M. Transparent Displays Enabled by Resonant Nanoparticle Scattering. *Nat. Commun.* **2014**, *5*, 3152.

(9) Li, N.; Yang, G.; Sun, Y.; Song, H.; Cui, H.; Yang, G.; Wang, C. Free-Standing and Transparent Graphene Membrane of Polyhedron Box-Shaped Basic Building Units Directly Grown Using a NaCl Template for Flexible Transparent and Stretchable Solid-State Supercapacitors. *Nano Lett.* **2015**, *15*, 3195−3203.

(10) Sollami Delekta, S.; Smith, A. D.; Li, J.; Ostling, M. Inkjet Printed Highly Transparent and Flexible Graphene Micro-Supercapacitors. *Nanoscale* **2017**, *9*, 6998−7005.

(11) Xu, P.; Kang, J.; Choi, J. B.; Suhr, J.; Yu, J.; Li, F.; Byun, J. H.; Kim, B. S.; Chou, T. W. Laminated Ultrathin Chemical Vapor Deposition Graphene Films Based Stretchable and Transparent High-Rate Supercapacitor. *ACS Nano* **2014**, *8*, 9437−9445.

(12) Jo, K.; Lee, S.; Kim, S.-M.; In, J. B.; Lee, S.-M.; Kim, J.-H.; Lee, H.-J.; Kim, K.-S. Stacked Bilayer Graphene and Redox-Active Interlayer for Transparent and Flexible High-Performance Supercapacitors. *Chem. Mater.* **2015**, *27*, 3621−3627.

(13) Zhong, Y.; Zhang, X.; He, Y.; Peng, H.; Wang, G.; Xin, G. Simultaneously Armored and Active Graphene for Transparent and Flexible Supercapacitors. *Adv. Funct. Mater.* **2018**, *28*, 1801998.

(14) Chen, T.; Xue, Y.; Roy, A. K.; Dai, L. Transparent and Stretchable High-Performance Supercapacitors Based on Wrinkled Graphene Electrodes. *ACS Nano* **2014**, *8*, 1039−1046.

(15) Qiu, T.; Luo, B.; Giersig, M.; Akinoglu, E. M.; Hao, L.; Wang, X.; Shi, L.; Jin, M.; Zhi, L. Au@MnO_2 Core−Shell Nanomesh Electrodes for Transparent Flexible Supercapacitors. *Small* **2014**, *10*, 4136−4141.

(16) Liu, Y.-H.; Xu, J.-L.; Gao, X.; Sun, Y.-L.; Lv, J.-J.; Shen, S.; Chen, L.-S.; Wang, S.-D. Freestanding Transparent Metallic Network Based Ultrathin, Foldable and Designable Supercapacitors. *Energy Environ. Sci.* **2017**, *10*, 2534−2543.

(17) Borysiewicz, M. A.; Ekielski, M.; Ogorzalek, Z.; Wzorek, M.; Kaczmarski, J.; Wojciechowski, T. Highly Transparent Supercapacitors Based on ZnO/MnO_2 Nanostructures. *Nanoscale* **2017**, *9*, 7577−7587.

(18) Wang, Y.; Zhou, W.; Kang, Q.; Chen, J.; Li, Y.; Feng, X.; Wang, D.; Ma, Y.; Huang, W. Patterning Islandlike MnO_2 Arrays by Breath-Figure Templates for Flexible Transparent Supercapacitors. *ACS Appl. Mater. Interfaces* **2018**, *10*, 27001−27008.

(19) Kiruthika, S.; Sow, C.; Kulkarni, G. U. Transparent and Flexible Supercapacitors with Networked Electrodes. *Small* **2017**, *13*, 1701906.

(20) Singh, S. B.; Singh, T. I.; Kim, N. H.; Lee, J. H. A Core−Shell MnO_2@Au Nanofiber Network as a High-Performance Flexible Transparent Supercapacitor Electrode. *J. Mater. Chem. A* **2019**, *7*, 10672−10683.

(21) Sheng, H.; Zhang, X.; Ma, Y.; Wang, P.; Zhou, J.; Su, Q.; Lan, W.; Xie, E.; Zhang, C. J. Ultrathin, Wrinkled, Vertically Aligned $Co(OH)_2$ Nanosheets/Ag Nanowires Hybrid Network for Flexible Transparent Supercapacitor with High Performance. *ACS Appl. Mater. Interfaces* **2019**, *11*, 8992−9001.

(22) Zhang, C. J.; Higgins, T. M.; Park, S.-H.; O'Brien, S. E.; Long, D.; Coleman, J. N.; Nicolosi, V. Highly Flexible and Transparent Solid-State Supercapacitors Based on RuO_2/PEDOT: PSS Conductive Ultrathin Films. *Nano Energy* **2016**, *28*, 495−505.

(23) Nam, I.; Park, S.; Kim, G.-P.; Park, J.; Yi, J. Transparent and Ultra-Bendable All-Solid-State Supercapacitors without Percolation Problems. *Chem. Sci.* **2013**, *4*, 1663−1667.

(24) Ma, D.; Ma, Y.; Chen, Z.; Hu, A. A Silk Fabric Derived Carbon Fibre Net for Transparent Capacitive Touch Pads and All-Solid Supercapacitors. *J. Mater. Chem. A* **2017**, *5*, 20608−20614.

(25) He, Y.; Chen, W.; Li, X.; Zhang, Z.; Fu, J.; Zhao, C.; Xie, E. Freestanding Three-Dimensional Graphene/MnO_2 Composite Networks as Ultralight and Flexible Supercapacitor Electrodes. *ACS Nano* **2013**, *7*, 174−182.

(26) Yuan, L.; Lu, X.-H.; Xiao, X.; Zhai, T.; Dai, J.; Zhang, F.; Hu, B.; Wang, X.; Gong, L.; Chen, J. Flexible Solid-State Supercapacitors Based on Carbon Nanoparticles/MnO_2 Nanorods Hybrid Structure. *ACS Nano* **2012**, *6*, 656−661.

(27) Liu, R.; Lee, S. B. MnO_2/Poly(3,4-ethylenedioxythiophene) Coaxial Nanowires by One-Step Coelectrodeposition for Electrochemical Energy Storage. *J. Am. Chem. Soc.* **2008**, *130*, 2942−2943.

(28) Wu, Z.-S.; Ren, W.; Wang, D.-W.; Li, F.; Liu, B.; Cheng, H.-M. High-Energy MnO_2 Nanowire/Graphene and Graphene Asymmetric Electrochemical Capacitors. *ACS Nano* **2010**, *4*, 5835−5842.

(29) Hou, Y.; Cheng, Y.; Hobson, T.; Liu, J. Design and Synthesis of Hierarchical MnO_2 Nanospheres/Carbon Nanotubes/Conducting Polymer Ternary Composite for High Performance Electrochemical Electrodes. *Nano Lett.* **2010**, *10*, 2727−2733.

(30) Chen, P.; Chen, H.; Qiu, J.; Zhou, C. Inkjet Printing of Single-Walled Carbon Nanotube/RuO_2 Nanowire Supercapacitors on Cloth Fabrics and Flexible Substrates. *Nano Res.* **2010**, *3*, 594−603.

(31) Decher, G. Fuzzy Nanoassemblies: Toward Layered Polymeric Multicomposites. *Science* **1997**, *277*, 1232−1237.

(32) Lee, J.-S.; Cho, J.; Lee, C.; Kim, I.; Park, J.; Kim, Y.-M.; Shin, H.; Lee, J.; Caruso, F. Layer-by-Layer Assembled Charge-Trap Memory Devices with Adjustable Electronic Properties. *Nat. Nanotechnol.* **2007**, *2*, 790−795.

(33) Podsiadlo, P.; Kaushik, A. K.; Arruda, E. M.; Waas, A. M.; Shim, B. S.; Xu, J.; Nandivada, H.; Pumplin, B. G.; Lahann, J.; Ramamoorthy, A.; Kotov, N. A. Ultrastrong and Stiff Layered Polymer Nanocomposites. *Science* **2007**, *318*, 80−83.

(34) Cho, J.; Char, K.; Hong, J. D.; Lee, K. B. Fabrication of Highly Ordered Multilayer Films Using a Spin Self-Assembly Method. *Adv. Mater.* **2001**, *13*, 1076−1078.

DOI: 10.1021/acsnano.9b04594
ACS Nano 2019, 13, 12719−12731

(35) Kim, S. Y.; Hong, J.; Kavian, R.; Lee, S. W.; Hyder, M. N.; Shao-Horn, Y.; Hammond, P. T. Rapid Fabrication of Thick Spray-Layer-by-Layer Carbon Nanotube Electrodes for High Power and Energy Devices. *Energy Environ. Sci.* **2013**, *6*, 888−897.
(36) Ko, Y.; Baek, H.; Kim, Y.; Yoon, M.; Cho, J. Hydrophobic Nanoparticle-Based Nanocomposite Films Using *In Situ* Ligand Exchange Layer-by-Layer Assembly and Their Nonvolatile Memory Applications. *ACS Nano* **2013**, *7*, 143−153.
(37) Park, M.; Kim, Y.; Ko, Y.; Cheong, S.; Ryu, S. W.; Cho, J. Amphiphilic Layer-by-Layer Assembly Overcoming Solvent Polarity between Aqueous and Nonpolar Media. *J. Am. Chem. Soc.* **2014**, *136*, 17213−17223.
(38) Cheong, S.; Kim, J.-K.; Cho, J. Functional Nanocomposites with Perfect Nanoblending between Water-Soluble Polymers and Hydrophobic Inorganic Nanoparticles: Applications to Electric-Stimuli-Responsive Films. *Nanoscale* **2016**, *8*, 18315−18325.
(39) Wu, Z. S.; Parvez, K.; Winter, A.; Vieker, H.; Liu, X.; Han, S.; Turchanin, A.; Feng, X.; Müllen, K. Layer-by-Layer Assembled Heteroatom-Doped Graphene Films with Ultrahigh Volumetric Capacitance and Rate Capability for Micro-Supercapacitors. *Adv. Mater.* **2014**, *26*, 4552−4558.
(40) Li, Z.; Wang, J.; Liu, X.; Liu, S.; Ou, J.; Yang, S. Electrostatic Layer-by-Layer Self-Assembly Multilayer Films Based on Graphene and Manganese Dioxide Sheets as Novel Electrode Materials for Supercapacitors. *J. Mater. Chem.* **2011**, *21*, 3397−3403.
(41) Sarker, A. K.; Hong, J. D. Layer-by-Layer Self-Assembled Multilayer Films Composed of Graphene/Polyaniline Bilayers: High-Energy Electrode Materials for Supercapacitors. *Langmuir* **2012**, *28*, 12637−12646.
(42) Hyder, M. N.; Gallant, B. M.; Shah, N. J.; Shao-Horn, Y.; Hammond, P. T. Synthesis of Highly Stable Sub-8 nm TiO2 Nanoparticles and Their Multilayer Electrodes of TiO2/MWNT for Electrochemical Applications. *Nano Lett.* **2013**, *13*, 4610−4619.
(43) Kim, Y.; Zhu, J.; Yeom, B.; Di Prima, M.; Su, X.; Kim, J.-G.; Yoo, S. J.; Uher, C.; Kotov, N. A. Stretchable Nanoparticle Conductors with Self-Organized Conductive Pathways. *Nature* **2013**, *500*, 59−63.
(44) Schmitt, J.; Decher, G.; Dressick, W. J.; Brandow, S. L.; Geer, R. E.; Shashidhar, R.; Calvert, J. M. Metal Nanoparticle/Polymer Superlattice Films: Fabrication and Control of Layer Structure. *Adv. Mater.* **1997**, *9*, 61−65.
(45) Sun, S. Recent Advances in Chemical Synthesis, Self-Assembly, and Applications of FePt Nanoparticles. *Adv. Mater.* **2006**, *18*, 393−403.
(46) Liu, L.; Guo, X.; Li, Y.; Zhong, X. Bifunctional Multidentate Ligand Modified Highly Stable Water-Soluble Quantum Dots. *Inorg. Chem.* **2010**, *49*, 3768−3775.
(47) Kanicky, J.; Poniatowski, A.; Mehta, N.; Shah, D. Cooperativity among Molecules at Interfaces in Relation to Various Technological Processes: Effect of Chain Length on the pKa of Fatty Acid Salt Solutions. *Langmuir* **2000**, *16*, 172−177.
(48) Liao, Q.; Li, N.; Cui, H.; Wang, C. Vertically-Aligned Graphene@MnO Nanosheets as Binder-Free High-Performance Electrochemical Pseudocapacitor Electrodes. *J. Mater. Chem. A* **2013**, *1*, 13715−13720.
(49) Messaoudi, B.; Joiret, S.; Keddam, M.; Takenouti, H. Anodic Behaviour of Manganese in Alkaline Medium. *Electrochim. Acta* **2001**, *46*, 2487−2498.
(50) Simon, P.; Gogotsi, Y. Materials for Electrochemical Capacitors. *Nat. Mater.* **2008**, *7*, 845−854.
(51) Li, R.-Z.; Peng, R.; Kihm, K.; Bai, S.; Bridges, D.; Tumuluri, U.; Wu, Z.; Zhang, T.; Compagnini, G.; Feng, Z.; Hu, A. High-Rate In-Plane Micro-Supercapacitors Scribed onto Photo Paper Using *In Situ* Femtolaser-Reduced Graphene Oxide/Au Nanoparticle Microelectrodes. *Energy Environ. Sci.* **2016**, *9*, 1458−1467.
(52) Wang, S.; Yu, Y.; Li, R.; Feng, G.; Wu, Z.; Compagnini, G.; Gulino, A.; Feng, Z.; Hu, A. High-Performance Stacked In-Plane Supercapacitors and Supercapacitor Array Fabricated by Femtosecond Laser 3D Direct Writing on Polyimide Sheets. *Electrochim. Acta* **2017**, *241*, 153−161.
(53) Tanggarnjanavalukul, C.; Phattharasupakun, N.; Kongpatpanich, K.; Sawangphruk, M. Charge Storage Performances and Mechanisms of MnO_2 Nanospheres, Nanorods, Nanotubes and Nanosheets. *Nanoscale* **2017**, *9*, 13630−13639.
(54) Sankar, K. V.; Selvan, R. K. The Preparation of $MnFe_2O_4$ Decorated Flexible Graphene Wrapped with PANI and Its Electrochemical Performances for Hybrid Supercapacitors. *RSC Adv.* **2014**, *4*, 17555−17566.
(55) Fan, Z.; Yan, J.; Zhi, L.; Zhang, Q.; Wei, T.; Feng, J.; Zhang, M.; Qian, W.; Wei, F. A Three-Dimensional Carbon Nanotube/Graphene Sandwich and Its Application as Electrode in Supercapacitors. *Adv. Mater.* **2010**, *22*, 3723−3728.
(56) Xu, K.; Li, W.; Liu, Q.; Li, B.; Liu, X.; An, L.; Chen, Z.; Zou, R.; Hu, J. Hierarchical Mesoporous $NiCo_2O_4$@MnO_2 Core−Shell Nanowire Arrays on Nickel Foam for Aqueous Asymmetric Supercapacitors. *J. Mater. Chem. A* **2014**, *2*, 4795−4802.
(57) Gallant, B. M.; Lee, S. W.; Kawaguchi, T.; Hammond, P. T.; Shao-Horn, Y. Electrochemical Performance of Thin-Film Functionalized Carbon Nanotube Electrodes in Nonaqueous Cells. *J. Electrochem. Soc.* **2014**, *161*, A1625−A1633.
(58) Andreas, H. A.; Black, J. M.; Oickle, A. A. Self-Discharge in Manganese Oxide Electrochemical Capacitor Electrodes in Aqueous Electrolytes with Comparisons to Faradaic and Charge Redistribution Models. *Electrochim. Acta* **2014**, *140*, 116−124.
(59) Lee, K.; Lee, H.; Shin, Y.; Yoon, Y.; Kim, D.; Lee, H. Highly Transparent and Flexible Supercapacitors using Graphene-Graphene Quantum Dots Chelate. *Nano Energy* **2016**, *26*, 746−754.
(60) Zhang, C.; Anasori, B.; Seral-Ascaso, A.; Park, S. H.; McEvoy, N.; Shmeliov, A.; Duesberg, G. S.; Coleman, J. N.; Gogotsi, Y.; Nicolosi, V. Transparent, Flexible, and Conductive 2D Titanium Carbide (MXene) Films with High Volumetric Capacitance. *Adv. Mater.* **2017**, *29*, 1702678.
(61) Park, J.; An, K.; Hwang, Y.; Park, J.-G.; Noh, H.-J.; Kim, J.-Y.; Park, J.-H.; Hwang, N.-M.; Hyeon, T. Ultra-Large-Scale Syntheses of Monodisperse Nanocrystals. *Nat. Mater.* **2004**, *3*, 891.
(62) Kanehara, M.; Koike, H.; Yoshinaga, T.; Teranishi, T. Indium Tin Oxide Nanoparticles with Compositionally Tunable Surface Plasmon Resonance Frequencies in the Near-IR Region. *J. Am. Chem. Soc.* **2009**, *131*, 17736−17737.
(63) Buttry, D. A. *Advances in Electroanalytical Chemistry: Applications of the QCM to Electrochemistry*; Marcel Dekker Inc.: New York, 1991; pp 1−82.
(64) Zhang, S.; Pan, N. Supercapacitors Performance Evaluation. *Adv. Energy Mater.* **2015**, *5*, 1401401.

DOI: 10.1021/acsnano.9b04594
ACS Nano 2019, 13, 12719−12731